Effect of upper airway on tracheobronchial fluid dynamics

Authors

Minsuok Kim,[1] Guilhem J. Collier,[2] Jim M. Wild,[2] Yongmann M. Chung[1]

Affiliations

[1]School of Engineering, University of Warwick, Coventry, UK

[2]Academic Unit of Radiology, Institute for In Silico Medicine, University of Sheffield Sheffield, UK.

Abbreviated title: Upper airway effect on the flow

Contact information

Dr. Yongmann M. Chung

School of Engineering, University of Warwick,

Gibbet Hill Road, Coventry CV4 7AL, UK

E-mail: Y.M.Chung@warwick.ac.uk

Phone: +44 (0)24 7657 4367, Fax: +44 (0)24 7641 8922

ABSTRACT

The upper airways play a significant role in the tracheal flow dynamics. Despite many previous studies, however, the effect of upper airways on the ventilation distribution in distal airways has remained a challenge. The aim of this study is to experimentally and computationally investigate the dynamic behaviour in the intra-tracheal flow induced by the upper respiratory tract and to assess its influence on the subsequent tributaries. Patient-specific images from two different modalities (MRI of the upper airways and CT of the lower airways) were segmented and combined. An experimental phantom of patient-specific airways (including the oral cavity, larynx, trachea, down to generations 6-8) was generated using 3D printing. The flow velocities in this phantom model were measured by the flow sensitized phase contrast MRI technique and compared to the computational fluid dynamics simulations. Both experimental and computational results show a good agreement in the time-averaged velocity fields as well as fluctuating velocity. The flows in the proximal trachea were complex and unsteady under both lower- and higher-flow rate conditions. CFD simulations were also performed with an airways model without the upper airways. Although the flow near the carina remained unstable only when the inflow rate was high, the influence of upper airways caused notable changes in distal flow distributions when the two airways models were compared with and without the upper airways. The results suggest that the influence of the upper airways should be included in the respiratory flow assessment as the upper airways extensively affect the flows in distal airways and consequent ventilation distribution in the lungs.

Keywords: Upper airway – trachea – MRI – CFD – flow – ventilation

INTRODUCTION

Recent progress in medical imaging and image-based modelling technique enables accurate flow assessments in patient-specific airways geometries [1-3]. Computational fluid dynamics (CFD) is a valid tool to assess the flow velocity and pressure in respiratory airways [4-10]. Patient-specific CFD modelling studies of central airway (from the trachea down to several generations) flows can describe the tracheal flow characteristics such as velocity profile, wall shear stress and pressure in detail [11-17]. Thorough literature reviews on the use of patient-specific CFD modelling can be found in [13, 14]. In the meantime, the importance of upper airways geometry has been often overlooked in past lung modelling studies, and this is partly because the upper airway is not routinely included in the scope of conventional lung imaging protocol in the radiological assessment of respiratory disease due to additional radiation exposure to patients [18, 19].

Instead, the flows in the human upper airways were modelled separately without lower airways in multiple studies [20-25]. Their modelling results revealed the complex and transient flow characteristics in the upper airways while the influence on the consecutive flows in the trachea was still less well understood. Recently, experimental and computational studies have included the upper airway geometries to elucidate the tracheobronchial flow dynamics [26-29]. Phuong et al. measured the flow velocities in a realistic replica of the human airway track using particle image velocimetry (PIV) under constant breathing conditions and compared to the Reynolds Averaged Navier-Stokes (RANS) computational fluid dynamics (CFD) simulations [26]. Lambert et al. performed a Large Eddy Simulation (LES) of the flows in a computed tomography (CT) based human airway model to show the left-right lung asymmetry of particle ventilation [27]. Calmet et al. conducted a large-scale

CFD simulation with an implicit LES model to highlight the unsteady flow characteristics during a rapid inhalation [28]. Banko et al. demonstrated the time-varying flow velocity field in an anatomically accurate experimental model using phase-contrast magnetic resonance velocimetry [29].

It was found from the previous modelling studies that the geometries of upper respiratory tracks (including the oral cavity, oropharynx and larynx) generated complex flow structures such as laryngeal jets, localised vortices and secondary flows followed by significant pressure drops and altered wall shear stress distributions in the tracheas. Their flow characteristics were different from the less skewed cross-sectional velocity profiles and simple flow patterns found in the lower airway only models [30-32]. Choi et al. demonstrated the formation of a laryngeal jet at the glottis in their LES model. The laryngeal jet fundamentally affected the turbulent flow characteristics in the trachea. [33]. The turbulent flow behaviour induced by the upper airway was gradually attenuated as the flow moves towards the distal branches. However, unsteady flow fluctuation was still discernible not only in the trachea but also in the primary and secondary bronchi [34]. While the local flow dynamics caused by the upper airway is well described in literature, the potential influence of upper airways affecting ventilation distribution in the lung has not been fully discussed yet.

This paper aims to investigate the tracheobronchial flow alterations caused by the upper airway geometry utilising a patient-specific CFD simulation. The combined airway (CA) models of upper and lower airway geometries are obtained from magnetic resonance imaging (MRI) and CT images from the same patient. The phase contrast velocimetry (PCV-MRI) has been used as a validation tool in vitro and in vivo studies [6, 29, 35, 37-39]. The pulmonary flow in a combined airway model is validated using PCV-MRI measurements. 3D steady and

2D/1D unsteady MRI flow measurements in the patient-specific airways model are compared with CFD simulations. CFD simulation results are also compared with and without the upper airways to illustrate their difference in tracheal flow characteristics and bronchial flow distribution. The effect of complex upper airway structure and the tracheal flow dynamics on the ventilation distribution in distal airways is discussed.

1. METHODS

1.1. Model geometry

A forty-nine-year-old female patient's imaging data was recruited in this study. The upper airway was segmented from the MRI images using ScanIP (Simpleware, Exeter, UK) while the lower airway model was reconstructed from the CT images using Mimics (Materialise, Leuven, Belgium). The segmented airway geometries were mutually registered and combined into a complete central airway model (Fig. 1). As a consequence, the resultant combined airway (CA) geometry consisted of the oral cavity, pharynx, larynx, trachea, primary bronchi, main bronchus, and up to the seventh generation of following local airway branches. It was noticeable that there was a significant constriction at the laryngeal airway. Based on the combined geometry of the airway model, a phantom model was 3D printed using the stereolithography technique (Materialise, Leuven, Belgium) and an MR-compatible material (TuskXC2700T / Tusk2700W, Tusk Somos®, Elgin, IL). In addition to the combined model of the upper and lower airways, we developed a lower airway (LA) geometry model to compare the computed flows with the CA model. The inlet boundary plane of the LA

geometry was defined with extra care to obtain similar flow conditions in the trachea to those in the CA model.

1.2. MRI Flow Measurements

The constant flow rate condition was used in the MRI flow measurement with water as a working fluid. Two different inflow rates (lower-flow, Q_L = 3.5 mL/s and higher-flow, Q_H = 20.0 mL/s) were used and they are equivalent to 55 mL/s and 314 mL/s of air flow rates to represent a quiet and a fast breathing, respectively. The corresponding Reynolds numbers ($Re = UD/\nu$) of the lower-flow (LF) and the higher-flow (HF) cases are Re = 350 and 2000, respectively. The flow velocities in the patient specific 3D printing model were measured by the flow sensitized phase contrast MRI technique [39]. 3D flow MRI measurements were performed on a 3 T MRI scanner (Philips, Ingenia, Netherlands) with a multi-channel cardiac coil during a constant flow of water (Q_L). The lung model was immersed in a water container. The oral cavity inlet was connected to a water reservoir and the flow was controlled by a constant height difference between the reservoir and a small diameter outlet in the container. Copper sulphate at the concentration of 15 mmol/L was added to the water to increase magnetic resonance signal. A 3D fast field echo sequence with flow encoding the gradients along the three axes was used with the following parameters: field of view of 200 mm × 160 mm × 250 mm, resolution of 0.39 mm × 0.39 mm × 1 mm, partial echo, echo time/repetition time of 3.9/7.8 ms, flip angle of 5˚. The acquisition was repeated twice with two different maximum velocity encoding values of 30 and 10 cm/s corresponding to an acquisition time of 12 and 15 minutes, respectively.

In addition to 3D flow measurements, 2D/1D velocity profiles measurements were performed on a 1.5 T scanner (GE, HDx, USA) with a birdcage head coil during a constant flow of water. A 2D Cartesian encoded spoiled gradient echo sequence with flow encoding gradient perpendicular to the slice orientation was implemented with the following parameters: field of view of 250 mm × 187.5 mm, resolution of 0.98 mm × 1.95 mm, slice thickness of 6 mm, flip angle of 60˚, echo time/repetition time of 7.9/15 ms. The acquisition time for each 2D slice was 2.9 s. Multiple slices from the trachea entrance to the trachea carina were acquired (see locations S1 to S5 in Fig. 1 and Table 1) for a full acquisition time of ~15 s. To obtain 1D successive velocity profiles, the sequence was repeated with phase encoding gradients off. The time resolution of two successive 1D velocity profiles was 30 ms. The experiments were repeated with different maximum velocity encoding gradients values of 20, 30 and 63 cm/s.

1.3. CFD Simulations and Data Analysis

The segmented model geometries were imported into Ansys ICEM CFD (Ansys, Abingdon, UK) for pre-processing. In order to achieve accurate flow assessments in the near wall region, seven prism layers were generated within the viscous sublayer while the rest of the space was filled by tetrahedral grids. The refinement levels of grids were determined from a grid independence study. A total of 4.8 and 11.3 million hybrid cells consisted of tetrahedrons and prism layers were generated for the LA and CA geometry models, respectively (Fig. 2). Two different inlet flow rates (Q_L and Q_H) were applied in the CFD simulations to model the experimental conditions. To provide the equivalent outlet boundary conditions as in the experiment, the constant pressure boundary condition was used at all outlets. The density and

dynamic viscosity of water in the CFD simulation were 997.56 kg/m^3 and 8.887 × 10^{-4} Pa·s, respectively. No-slip and rigid boundary conditions were imposed on the airway wall.

The finite volume based CFD code, Ansys CFX (Ansys, Abingdon, UK) was used to solve the unsteady, incompressible Navier-Stokes equations. While the boundary condition applied is to model the constant inhalation, the flow can become unsteady due to the physiological geometry of the upper airways. The pressure and velocity in the governing equations were solved in a finite volume domain and the PISO algorithm for the coupling. The equations were discretised using second-order accurate schemes. An implicit second-order accurate time differencing scheme is used for the transient flows. The convergence was achieved by reducing all flow residuals to less than 10^{-5}. Since the low-Reynolds number nature of the flows in most of branches, the laminar flow model was used for the lower-flow condition (Re = 300). However, the localised turbulence due to the presence of a strong laryngeal jet was observed in the larynx region under the higher-flow condition, an LES model was used for the higher-flow conditions (Re = 2000). In LES, the subgrid-scale eddies were modelled with the wall-adapting local eddy-viscosity model (WALE) while the large-scale eddies were calculated by the filtered Navier-Stokes equations [40].

For the unsteady simulation, a time step size of 1 millisecond was used, and the simulation was performed for 21 seconds. This simulation time was long enough to observe fully developed state. The first 18 seconds of simulation results were discarded to remove the initial transient caused by the initial CFD condition, and the time averaging was performed for the last three seconds. All the computations were carried out on the high performance computing cluster (Lenovo NeXtScale nx360 M5 servers with 2 x Intel Xeon E5-2630 v3 2.4

GHz Haswell 8-core processors; 16 cores per node; 203 nodes; 3488 cores; 64 GB DDR4 memory per node / 4 GB per core) at the University of Warwick.

Once the computations of flow properties were completed, the CFD datasets were manually registered and compared to the MRI measurements. For the combined airway geometry with lower-flow (CA-LF) case, the time-averaged velocity fields on the cross-sectional planes (S1-S8 in Fig. 1 and Table 1) in the CFD simulation were compared to those in the PCV-MRI measurements. Moreover, the local flow rates at twelve different locations in the trachea and main bronchi were compared between the CFD and MRI results.

Since the flow in the coupled airway geometry in the higher-flow (CA-HF) case is expected to be highly unsteady depending on its location, the variation of the flow velocity profiles as well as the flow distribution on the cross-sectional planes (S1-S4 in Table 1) in the trachea is illustrated. Here, the velocity profiles over the cross-sectional planes in the CA-HF case were obtained by line averaging of the normal flow velocities from the anterior to posterior direction.

In addition to the flow fields, the spectral energy of the dynamic flow was analysed to elucidate the development of the turbulent characteristics in the tracheal flow from the CA-HF CFD simulation. The Kolmogorov's energy spectrum of turbulence (E) in the inertial subrange where the energy density depends only on the scale (k) and energy dissipation rate (ε) becomes

$$E(k) = C \cdot \varepsilon^{\frac{2}{3}} \cdot k^{-\frac{5}{3}}, \quad (1)$$

where C is a constant and k is the wave number. The characteristics of power spectra of the kinetic energy in the flows at three different locations (centre points on the cross-sectional planes, S2-S4) in the trachea are presented in this study.

To clarify the effect of the upper airway on the tracheal flow, the flows in the lower-airway-only geometry model were also simulated for lower-flow (LA-LF) and higher-flow (LA-HF) cases. The temporal flow distributions on the coronal plane in the LA geometry models were compared to those in the CA models. In addition to the temporal flow characteristics in the trachea, the dynamic flow split ratios of the tracheal flows into the right main bronchus were compared between the LA and CA models. Furthermore, the flows in the full airway networks in both models were visualised to distinguish the influence of upper airway on the distal airway flow distribution.

2. RESULTS

2.1. Combined airway (CA) results

It is found that the tracheal flows in the CA-LF case of the MRI and CFD are almost steady with very small fluctuations. Figure 3 illustrating the time-averaged flow velocity fields on the cross-sectional planes reveals a great resemblance between the MRI and CFD. The flows in the upper airway tract are deflected by the posterior wall of the curved airway at the oropharynx and consecutively encounter a laryngeal constriction. The narrowing of air pathway before trachea increases the flow velocity and decreases the pressure. Consequently, the increased flow velocity by the laryngeal constriction provokes the formation of the jet stream in the trachea (S8). The cross-sectional flow field in the proximal trachea shows skewed distribution to have a fast flow near the anterior wall (S1). This distribution gradually

develops as the flow moves downstream and becomes nearly axisymmetric at the distal trachea (S3-4) due to the low *Re* nature of the flow in the LF case. The tracheal flow splits into two at the carina of the trachea and goes furthers down to the left and right main bronchi (S5-7). In addition to the tracheal flow distribution, shown in Figure 4 and Table 2 are the flow rates in the trachea and main bronchi in the CA-LF case. Again, the local flow data reveal an excellent agreement between the MRI measurement and the CFD analysis. It is notable that more flow goes into the right main bronchus then the left in both MRI and CFD results.

Tracheal flow distributions on the cross-sectional planes in the CA-HF case are demonstrated in Figure 5(a). There are differences in the boundary shapes of the flow fields on the proximal cross-sections, S1 and S2, between the MRI and CFD because the minimal flow velocities (< 0.5 cm/s for S1 and < 0.1 cm/s for S2) are shown in white colour in the MRI, while those are dark blue in the CFD. Despite those differences, the MRI and CFD flow velocity contours reveal substantial similarity. The flow distribution is skewed to the anterior wall to form a strong jet in the proximal trachea (S1-2) and disperse to the larger area in the downstream trachea as it is previously shown in the CA-LF case.

Figure 5(b) illustrates the transition of temporal flow velocity profiles in the CA-HF case. The velocity profiles reveal the flows in the upstream trachea (S1-S2) are highly unsteady with significant variations and the temporal flow distributions on these planes are frequently biased. However, the dynamic characteristics of the flow are gradually attenuated as the flow moves to the distal trachea (S3-4). In summary, table 3 shows the changes in the mean flow velocity and standard deviation of the velocity profiles along the trachea. Both mean velocity and standard deviations from the MRI and CFD results decrease as the flow

moves to the downstream trachea. The variations of the temporal velocity profiles in the CFD simulation are smaller than those in the MRI measurements.

As the tracheal flows in the CA model are transient, the spectral energy distribution of the dynamic flows is computed at three different locations along the trachea (S2-4) from the CA CFD simulation. Figure 6 demonstrates the spectral kinetic energy distribution of the tracheal flow. The slope of energy dissipation at the proximal trachea (S2) reveals the existence of the inertial subrange (-5/3 range) of turbulent flow and the viscous dissipation (-7 range) in the CA-HF case while the flow in the CA-LF case remains virtually laminar with very small kinetic energy. The turbulent kinetic energy is reduced further downstream at S3-4. Consequently, the turbulent flow activity is substantially weakened in the distal trachea (S4) even though the flow is still turbulent at the distal trachea in the CA models. In contrast, the kinetic energy of the tracheal flow in the LA-LF and LA-HF cases are very small, less 0.002% and 0.004% of the mean flow velocity, respectively.

2.2. Lower airway (LA) results

To shed light on the effect of the upper airway on the flows in the trachea and main bronchi, CFD simulation results are compared between the LA and CA models. Figure 7 shows the temporal flow distributions on the coronal planes in the CFD simulations. The LA geometry model demonstrates much smoother and almost steady flow distributions in the trachea, while the tracheal flows in the CA geometry model are more complex and transient compared to the LA case. The skewed flow distribution induced by the laryngeal jet in the CA-LF case is widely disseminated and disappears near the carina of the trachea. Meanwhile, the CA-HF case shows irregular and chaotic flow distribution in the entire trachea. The tracheal flows are split by the carina and enter the right or left main bronchi. Thus, the

dynamic flow characteristics in the distal trachea directly affect the flows in the right and left main bronchi and even possibly interfere with the flows in subsequent branches.

Figure 8 depicts the ratio of the tracheal flow into the right main bronchus in the CFD simulation. The tracheal flows in all cases are biased towards the right main bronchus (> 0.5) as it is found in Fig. 4 from the MRI flow measurement in the CA-LF case. The biased flow ratios are more significant (1.5-2%) in the HF cases compared to the LF cases. It is notable that the flow ratios in the LA cases are almost steady regardless of the flow condition. Even though the flow ratio in the CA-LF case changes slowly, it shows a close resemblance to the LA-LF case. Whereas, the flow in the CA-HF case constantly fluctuates and the average flow ratio is slightly (0.3-2.3%) lower than the LA-HF case.

In addition to the dynamic flow behaviours in the main bronchus, the time-averaged flow distributions over the entire airway networks in the CFD simulations are illustrated in Figure 9. The boxes in this figure depict the airway elements from the trachea to the terminal branches in the simulation. The width of each box demonstrates the flow rate which confirms that the flow in a parent branch is equivalent to the summation of two descending branch flows. The colour of the boxes shows the ratio of the local airway flow to the tracheal flow. The number of terminal branches increases from left to the right. We marked only multiples of five in the plots. This figure illustrates the biased flows in the trachea to more likely enter the right main bronchus. It also shows the influence of the upper airway on distal airway flows. There are similarities in the flow distribution between the LF cases (Figs. 9 (a) and (b)), and HF cases (Figs. 9 (c) and (d)) which are geometrically identical despite their difference in flow scales due to the boundary conditions. However, the effect of upper airway increases the flows into the RUL and LLL in the CA cases. It subsequently affects the distal airway flows.

Figure 10 clearly illustrates the flow rates at the bronchial elements in the LA and CA cases. The data demonstrates the similarity in the proximal airway flows (Gen 3-4) between the LA and CA cases gradually diminishes as the flow propagates to the middle (Gen 5-6) and the distal airways (Gen 7-10).

3. DISCUSSION

The measurement uncertainty in standard MR imaging is usually defined by the image signal to noise (SNR) ratio. In the MRI flow measurement, however, the quantification of uncertainty is more complex since the velocity is encoded in the phase of the signal and not in the magnitude. The velocity measurement error is directly proportional to the pixel velocity and inversely proportional to the choice of maximum velocity encoding value [41]. In the 3D measurement of the lower flow model, the experiment was repeated twice with two different maximum velocity encoding values: 30 cm/s to avoid phase wrapping in the upper airways and 10 cm/s to improve the velocity to noise ratio in the regions with low velocities. In vitro experiments like the one we are reporting in this paper offer the possibility to repeat the measurement several times and optimize signal and velocity to noise ratio through careful choice of sequence parameters. The resulting velocity errors are therefore usually small and can be negligible compared to hardware related sources of error. The latter consists of eddy currents, Maxwell terms and gradient field inhomogeneities [42] that are strongly dependent on scanner model hardware due to the difference in gradient coil design, maximum gradient strength and slew rate. As an indication of the velocity measurement uncertainty to be expected in our measurement, Giese et al. [43] estimated the velocity error to be less than 2.5% for a system similar to our (3T Philips Achieva system). The velocity errors are also

dependent on object geometry and dimension, with minimum uncertainty in the isocentre of the magnet (corresponding to the centre of the trachea in our experiment) and increasing errors at the periphery of the lung model.

A curved and irregularly shaped upper airway tract has been known to bring radical alternations in the tracheobronchial flow dynamics. The narrow larynx and resulting unsteady jet formation contribute to the biased flow distribution on the cross-sectional planes while the curved airway structure is most likely responsible for the secondary flow generation [44]. The current CFD simulations and MRI measurements enabled us to confirm the appearance of complex tracheal flow characteristics induced by the upper airway such as the laryngeal jet, biased cross-sectional airway flow distribution, secondary flow, and dynamic velocity profiles which have been illustrated in previous modelling studies [24, 26, 29, 34]. Those complex flow behaviours are highly dependent on the airway geometry as well as the flow rate. Lin et al. [45] showed the laryngeal jet biased towards posterior wall of their realistic subject-specific upper respiratory tract model. By contrast, it was biased towards to anterior wall in other studies [46, 47] as we found in both CFD and experimental analyses of our CA models. The disturbed flow patterns in the upstream trachea appeared in both LF and HF cases, but the behaviours of the downstream tracheal flows were different from each other. The laryngeal jets in the CA-HF case were strong and highly unstable compared to the weak and steady jets in the CA-LF case and it affected to the subsequent flows in the main bronchi.

In an earlier study, Luo and Liu [48] extended and modified the trachea geometry to have a biased tracheal flow velocity profile to simulate the effect of a laryngeal jet. In their conclusions, the flow ratio to the left and right lobes was insensitive to the *Re* number. We partly agree with those conclusions. As it was previously discussed, the flows at downstream trachea in the CA-HF case were highly unsteady and subsequent flow ratios to the right lobes

were variable. Moreover, the time-averaged flow ratios in the high *Re* (CA-HF) and low *Re* (CA-LF) cases were different. These results illustrated the tracheal flow split ratio could be sensitive to the *Re* number. We presume that some of the key flow characteristics such as secondary flows and vortices at the tracheal inlet could hardly be included in their model with the modified geometries. If so, the simplified inlet flow boundary assumptions could result in the different flow behaviours compared to the models with realistic upper airway geometry in the current study.

We showed that the tracheal flow ratios to the main bronchi are different between the LA-HF and CA-HF cases. Relatively, the difference was minimal for the LF cases as the effect of upper airway provoking flow perturbations almost diminished at the downstream trachea. However, even though they were small in the upstream airways (G3-4), the flow rate discordances between the LA and CA cases increased rapidly as the flow moved towards the tributary. Consequently, the flow rates in those models became significant in the distal branches (G7-10). These results demonstrated a nature of cumulative error reproduction in an assessment of ventilation distribution within an airway network system due to its branching structure. Thus, minor alterations at the airway boundary of a model could result in notable distortions in tributary flows regardless of breathing conditions.

Complex flow patterns and contorted air pathways incited by an upper airway tract could extend the travel distance and the residence time of the inspired particles. Accordingly, the particles could have more chance to impact the airway wall. Multiple studies have shown the relationship between the *Re* number and particle deposition [49, 50]. Luo and Lin demonstrated the significantly increased amount of particle deposition in the turbulent flow models compared to the laminar flow models [48]. Lambert et al. found that the particle-

laden turbulent laryngeal jet caused a disproportion of particle split to go into the primary bronchi and succeeding branches [27]. The particle transport and deposition models were not included in the current study. Nonetheless, we confirmed the turbulent flow characteristics in the upstream trachea and unsteady flow behaviours in the main bronchi in the CA-HF case. In addition, as it was aforementioned, the upper airway still affected the flow distribution in distal airways despite the inspiratory flow rate was low. These results allow us to deduce that the upper airway directly makes an impact on the particle deposition on the trachea and main bronchi if the flow rate is high, while it extensively affects the particle distribution in small airways when the flow rate is low.

We assumed the airway walls in the CFD simulations were rigid. It was a fair assumption to model the surface of the experimental phantom but different from the physiological airway wall. In spite of the difference, the interaction of airflow and compliant airway wall was considered negligible so that the rigid wall assumption has been widely accepted in previous CFD studies to model the airway flows. Furthermore, we decided that the small-scale peripheral airways and acini models were beyond the scope of the current study. As a consequence, the pressures at the outlet boundaries were simplified to be uniformly constant without the influence from the peripheral airway flows and compliant acinar dynamics. Again, those boundary assumptions were similar to the experimental conditions for the MRI flow measurements but could limitedly represent the variant flow conditions in the patient-specific airway geometry. One of the options to improve the outlet boundary assumptions in the current models could be using a full-scale conducting airway model [31, 51]. It could allow assessing the upper airway effects on the flows in an extended range of branches and possibly on a whole lung ventilation. Further studies need to be performed to clarify those.

4. CONCLUSIONS

The effects of upper airways on tracheal flow dynamics in a patient-specific airway model are assessed using MRI flow measurement and CFD analysis. The experimental MRI measurements and CFD simulation results show good agreement with each other. The upper airway morphology and the laryngeal constriction enhance the turbulent kinetic energy in the upstream tracheal flows. The impact is weakened in the downstream branches but the flows in the distal trachea are still complex and unsteady when the flow rate is high. The small difference in the main bronchial flows between the LA and CA cases increased in the distal bronchi. The results suggest that the influence of upper airways on the flows in the trachea and tributaries may significantly affect the ventilation distribution of a lung. We conclude that flow in the upper airways needs to be borne in mind when performing CFD analyses of ventilation distribution as well as particle deposition in the airways of the lungs.

ACKNOLEDGEMENTS

This work was funded by a European Union Seventh Framework grant, AirPROM (www.airprom.eu), grant agreement no. 270194; the Medical Research Council (MRC) and the National Institute of Health Research (NIHR). The 3D printed phantom model was supported by the Materialize. The support from the UK Turbulence Consortium (EP/L000261/1) is also acknowledged. The views expressed are those of the authors and not

necessarily those of the National Health Service (NHS), the NIHR or the Department of Health.

REFERENCES

1. Saksono PH, Nithiarasu P, Sazonov I, Yeo SY. Computational flow studies in a subject-specific human upper airway using a one-equation turbulence model. Influence of the nasal cavity. *Int J Numer Meth Eng*. 2011;**87**:96–114.
2. Vinchurkar S, De Backer L, Vos W, Van Holsbeke C, De Backer J, De Backer W. A case series on lung deposition analysis of inhaled medication using functional imaging based computational fluid dynamics in asthmatic patients: effect of upper airway morphology and comparison with in vivo data. *Inhal Toxicol*. 2012;**24**(2):81-88.
3. Kim M, Bordas R, Brightling C, Chung YM. Dynamic flows in the coupled model of 1D and 3D CFD. *Eur Respir J*. 2016;**48**:PA4403.
4. Suh Y, Park JY. Effect of off-plane bifurcation angles of primary bronchi on expiratory flows in the human trachea. *Comput Biol Med*. 2018;**95**:63–74.
5. Bauer K, Rudert A, Brücker C. Three-dimensional flow patterns in the upper human airways. *J Biomech Eng*. 2012;**134**(7):071006.
6. Minard KR, Kuprat AP, Kabilan S, et al. Phase-contrast MRI and CFD modeling of apparent ^{3}He gas flow in rat pulmonary airways. *J Magn Reson*. 2012;**221**:129–138.
7. Yin Y, Choi J, Hoffman EA, Tawhai MH, Lin CL. Simulation of pulmonary air flow with a subject-specific boundary condition. *J Biomech*. 2010;**43**(11):2159–2163.
8. Gemci T, Ponyavin V, Chen Y, Chen H, Collins R. Computational model of airflow in upper 17 generations of human respiratory tract. *J Biomech*. 2008;**41**(9):2047–2054.
9. de Backer JW, Vos WG, Gorlé CD, et al. Flow analyses in the lower airways: patient-specific model and boundary conditions. *Med Eng Phys*. 2008;**30**(7):872–879.

10. Ma B, Lutchen KR. An anatomically based hybrid computational model of the human lung and its application to low frequency oscillatory mechanics. *Ann Biomed Eng*. 2006;**34**(11):1691–1704.
11. Qi S, Li Z, Yue Y, Van Triest HJW, Kang Y. Computational fluid dynamics simulation of airflow in the trachea and main bronchi for the subjects with left pulmonary artery sling. *Biomed Eng Online*. 2014;**13**(85). doi:10.1186/1475-925X-13-85.
12. Malvè M, Del Palomar AP, Chandra S, et al. FSI analysis of the human trachea under impedance-based boundary conditions. *J Biomech Eng*. 2011;**133**(2):021001.
13. Tawhai MH, Lin CL. Airway gas flow. *Compr Physiol*. 2011;**1**(3):1135–1157.
14. Kleinstreuer C, Zhang Z. Airflow and particle transport in the human respiratory system. *Annu Rev Fluid Mech*. 2010;**42**(1):301–334.
15. Freitas RK, Schröder W. Numerical investigation of the three-dimensional flow in a human lung model. *J Biomech*. 2008;**41**(11):2446–2457.
16. van Ertbruggen C, Hirsch C, Paiva M. Anatomically based three-dimensional model of airways to simulate flow and particle transport using computational fluid dynamics. *J Appl Physiol*. 2005;**98**(3):970–980.
17. Cebral JR, Summers RM. Tracheal and central bronchial aerodynamics using virtual bronchoscopy and computational fluid dynamics. *IEEE Trans Med Imaging*. 2004;**23**(8):1021–1033.
18. Ma B, Lutchen KR. CFD simulation of aerosol deposition in an anatomically based human large-medium airway model. *Ann Biomed Eng*. 2009;**37**(2):271-285.
19. Ball CG, Uddin M, Pollard A. High resolution turbulence modelling of airflow in an idealised human extra-thoracic airway. *Comput Fluids*. 2008;**37**(8):943–964.

20. Wei W, Huang S, Chen L, Qi Y, Qiu Y, Li S. Airflow behavior changes in upper airway caused by different head and neck positions: Comparison by computational fluid dynamics. *J Biomech*. 2017;**52**:89-94.
21. Bates AJ, et al. Assessing the relationship between movement and airflow in the upper airway using computational fluid dynamics with motion determined from magnetic resonance imaging. *Clin Biomech*. 2017. doi:10.1016/j.clinbiomech.2017.10.011.
22. Pirnar J, Dolenc-Grošelj L, Fajdiga I, Žun I. Computational fluid-structure interaction simulation of airflow in the human upper airway. *J Biomech*. 2015;**48**:3694-3700.
23. Lu MZ, Liu Y, Ye JY, Luo HY. Large eddy simulation of flow in realistic human upper airways with obstructive sleep. *Procedia Comput Sci*. 2014; **29**:557-564.
24. Mylavarapu G, Murugappan S, Mihaescu M, Kalra M, Khosla S, Gutmark E. Validation of computational fluid dynamics methodology used for human upper airway flow simulations. *J Biomech*. 2009;**42**(10):1553–1559.
25. Nithiarasu P, Hassan O, Morgan K. Steady flow through a realistic human upper airway geometry. *Int J Numer Meth Fluids*. 2008;**57**:631–651.
26. Phuong NL, Ito K. Investigation of flow pattern in upper human airway including oral and nasal inhalation by PIV and CFD. *Build Environ*. 2015;**94**:504-515.
27. Lambert AR, O'Shaughnessy P, Tawhai MH, Hoffman EA, Lin CL. Regional deposition of particles in an image-based airway model: large-eddy simulation and left-right lung ventilation asymmetry. Aerosol Sci Technol. 2011;**45**(1):11-25.
28. Calmet H, Gambaruto AM, Bates AJ, Vázquez M, Houzeaux G, Doorly DJ. Large-scale CFD simulations of the transitional and turbulent regime for the large human airways during rapid inhalation. *Comput Biol Med*. 2016;**69**:166-180.

29. Banko AJ, Coletti F, Elkins CJ, Eaton J. Oscillatory flow in the human airways from the mouth through several bronchial generations. *Int J Heat Fluid Flow*. 2016;**61**:54-57.
30. Qi S, Zhang B, Yue Y, et al. Airflow in tracheobronchial tree of subjects with tracheal bronchus simulated using CT image based models and CFD method. *J Med Syst*. 2018;**42**(4):65.
31. Ismail M, Comerford A, Wall WA. Coupled and reduced dimensional modeling of respiratory mechanics during spontaneous breathing. *Int J Numer Method Biomed Eng*. 2013;**29**(11):1285–1305.
32. Saber EM, Heydari G. Flow patterns and deposition fraction of particles in the range of 0.1–10 μm at trachea and the first third generations under different breathing conditions. *Comput Biol Med*. 2012;**42**(5):631–638.
33. Choi J, Tawhai MH, Hoffman EA, Lin CL. On intra- and intersubject variabilities of airflow in the human lungs. *Phys Fluids*. 2009;**21**:101901.
34. Bernate JA, Geisler TS, Padhy S, Shaqfeh ESG, Iaccarino G. Study of the flow unsteadiness in the human airway using large eddy simulation. *Phys Rev Fluids*. 2017;**2**:083101.
35. Collier GJ, Wild JM. In vivo measurement of gas flow in human airways with hyperpolarized gas MRI and compressed sensing. *Magn Reson Med*. 2015;**73**(6):2255-2261.
36. Collier GJ, Kim M, Chung YM, Wild JM. 3D phase contrast MRI in models of human airways - validation of computational fluid dynamics simulations of steady inspiratory flow. *JMRI*. 2018. doi: 10.1002/jmri.26039.

37. Banko AJ, Coletti F, Schiavazzi D, Elkins CJ, Eaton JK. Three-dimensional inspiratory flow in the upper and central human airways. *Exp Fluids*. 2015;**56**(6):117.
38. de Rochefort L, Vial L, Fodil R, et al. In vitro validation of computational fluid dynamic simulation in human proximal airways with hyperpolarized 3He magnetic resonance phase-contrast velocimetry. *J Appl Physiol*. 2007;**102**(5):2012–2023.
39. de Rochefort L, Maître X, Fodil R, et al. Phase-contrast velocimetry with hyperpolarized 3He for in vitro and in vivo characterization of airflow. *Magn Reson Med*. 2006;**55**(6):1318–1325.
40. Nicoud F, and Ducros F. Subgrid-scale stress modelling based on the square of the velocity gradient tensor. *Flow Turbul Combust*. 1999;**62**(3):183-200.
41. Elkins CJ, and Alley MT. Magnetic resonance velocimetry: applications of magnetic resonance imaging in the measurement of fluid motion. *Exp Fluids*. 2007;**43**(6):823–858.
42. Lorenz R, Bock J, Snyder J, Korvink JG, Jung BA, Markl M. Influence of eddy current, Maxwell and gradient field corrections on 3D flow visualization of 3D CINE PC-MRI data. *Magn Reson Med*. 2014;**72**(1):33-40.
43. Giese D, Haeberlin M, Barmet C, Pruessmann KP, Schaeffter T, Kozerke S. Analysis and correction of background velocity offsets in phase-contrast flow measurements using magnetic field monitoring. *Magn Reson Med*. 2012;**67**(5):1294-302.
44. Kim J, Yadav M, Kim S. Characteristics of secondary flow induced by 90-degree elbow in turbulent pipe flow. *Eng Appl Comp Fluid*. 2014;**8**(2):229-239.
45. Lin CL, Tawhai MH, McLennan G, Hoffman E. Characteristics of the turbulent laryngeal jet and its effect on airflow in the human intra-thoracic airways. *Respir Physio Neurobiol*. 2007;**157**(2–3):295–309.

46. Zhang Z, Kleinstreuer C. Airflow structures and nano-particle deposition in a human upper airway model. *J Comput Phys*. 2004;**198**(1):178-210.
47. Phuong NL, Ito K. Investigation of flow pattern in upper human airway including oral and nasal inhalation by PIV and CFD. *Build Environ*. 2015;**94**:504-515.
48. Luo HY, Liu Y. Particle deposition in a CT-scanned human lung airway. *J Biomech*. 2009;**42**(12):1869–1876.
49. Koullapis PG, Kassinos SC, Bivolarova MP, Melikov AK. Particle deposition in a realistic geometry of the human conducting airways: Effects of inlet velocity profile, inhalation flowrate and electrostatic charge. *J Biomech*. 2016;**49**(11):2010-2212.
50. Wilson SR, Liu Y, Matida EA, Johnson MR. Aerosol deposition measurements as a function of Reynolds number for turbulent flow in a ninety-degree pipe bend. *Aerosol Sci Technol*. 2011;**45**(3):364-375.
51. Kim M, Bordas R, Vos W, et al. Dynamic flow characteristics in normal and asthmatic lungs. *Int J Numer Method Biomed Eng*. 2015;**31**(12):e02730.

TABLES

Table 1. Locations of cross-sectional planes.

Cross section ID	Location
S0	Larynx opening
S1	After the larynx opening
S2	Beginning of trachea
S3	Middle of trachea
S4	A few centimetres above carina
S5	Carina bifurcation
S6	Right main bronchus
S7	Left main bronchus
S8	Sagittal middle cut of trachea

* Locations of the tracheal cross sections (S1-4) in the higher-flow (HF) model are 5 *mm* closer to the larynx than those in the lower-flow (LF) model.

Table 2. Flow rates at different locations in the MRI measurements and CFD simulations.

Location	MRI	CFD
Trachea after uvula	3.16	3.46
Trachea before carina	3.52	3.5
Right main bronchus	1.82	1.94
Left main bronchus	1.68	1.55
Left lower lobe bronchus	0.68	0.59
Truncus intermedius	0.82	0.94
Left upper lobe	0.69	0.64
Left lower lobe	0.94	0.82
Right upper lobe	1.0	0.89
Right middle lobe	0.2	0.16
Right lower lobe 1	0.8	0.77
Right lower lobe 2	0.04	0.03

(Unit: *ml/s*)

Table 3. Changes in the mean and standard deviation of the velocity profile along the trachea

Cross section ID	Distance from S1 (cm)	MRI (cm/s)	CFD (cm/s)
S1	0	21.6 ± 6.1	23.8 ± 4.8
S2	2.2	15.4 ± 3.6	15.5 ± 2.3
S3	4.5	12.4 ± 1.8	11.4 ± 1.6
S4	6.9	11.3 ± 1.3	10.4 ± 1.3

FIGURE LEGENDS

Figure 1. A schematic illustration of the CFD analysis and the MRI flow measurement. Cross-sectional planes to measure flow velocities are indicated in the lower left, MR image based flow measure picture (S1-S8). Larynx is located above the cross-sectional plane, S1.

Figure 2. CFD grids for the CA model (left and middle: surface grids, right: interior volume grids appearing on cross-sectional planes at proximal and distal trachea).

Figure 3. Flow velocity fields on the cross-sectional planes (S1 - S8) in the CA-LF case. Anatomical directions, anterior (A) and posterior (P), are indicated on the first contour plot (S1-MRI).

Figure 4. Comparison of flow rates at different locations (2 trachea, 2 main bronchi, 8 lobar/distal bronchi) between the MRI and CFD results in the CA-LF case.

Figure 5. Tracheal flow characteristics in the CA-HF case. (a) Time-averaged velocity field, and (b) temporal velocity profiles (black solid lines), time averaged velocity profile (red solid lines) and standard deviations (red dashed lines) on the cross-sectional plan.

Figure 6. Kinetic energy spectra of tracheal flows at three different locations (centre of the S2-4) in the CA cases. The straight dashed line indicates Kolmogorov's law (-5/3 range). (a) CA-LF case, and (b) CA-HF case.

Figure 7. Temporal flow velocity fields on the coronal planes in the CFD

simulations at two different instants of time (t1 and t2). (a) LA model, and (b) CA model.

Figure 8. Ratio of the tracheal flow into the right main bronchus ($Q_{right}/Q_{trachea}$).

Figure 9. Time-averaged flow distribution of the CFD simulations. (a) LA-LF, (b) CA-LF, (c) LA-HF, (d) CA-HF model. Terminal branch numbers of the boxes in the flow distribution plots increase from the left to the right as the circled numbers indicate. The corresponding branches, as well as a full set of terminal branch numbers, are shown in the right-hand side tree picture. The colour of each box indicates the partitioning to the tracheal flow.

Figure 10. Comparison of the time averaged flow rates in the proximal (Generation 3-4), middle (5-6) and distal (7-10) bronchi between the LA and CA models. (a) LF model, (b) HF model.

Figure 1.

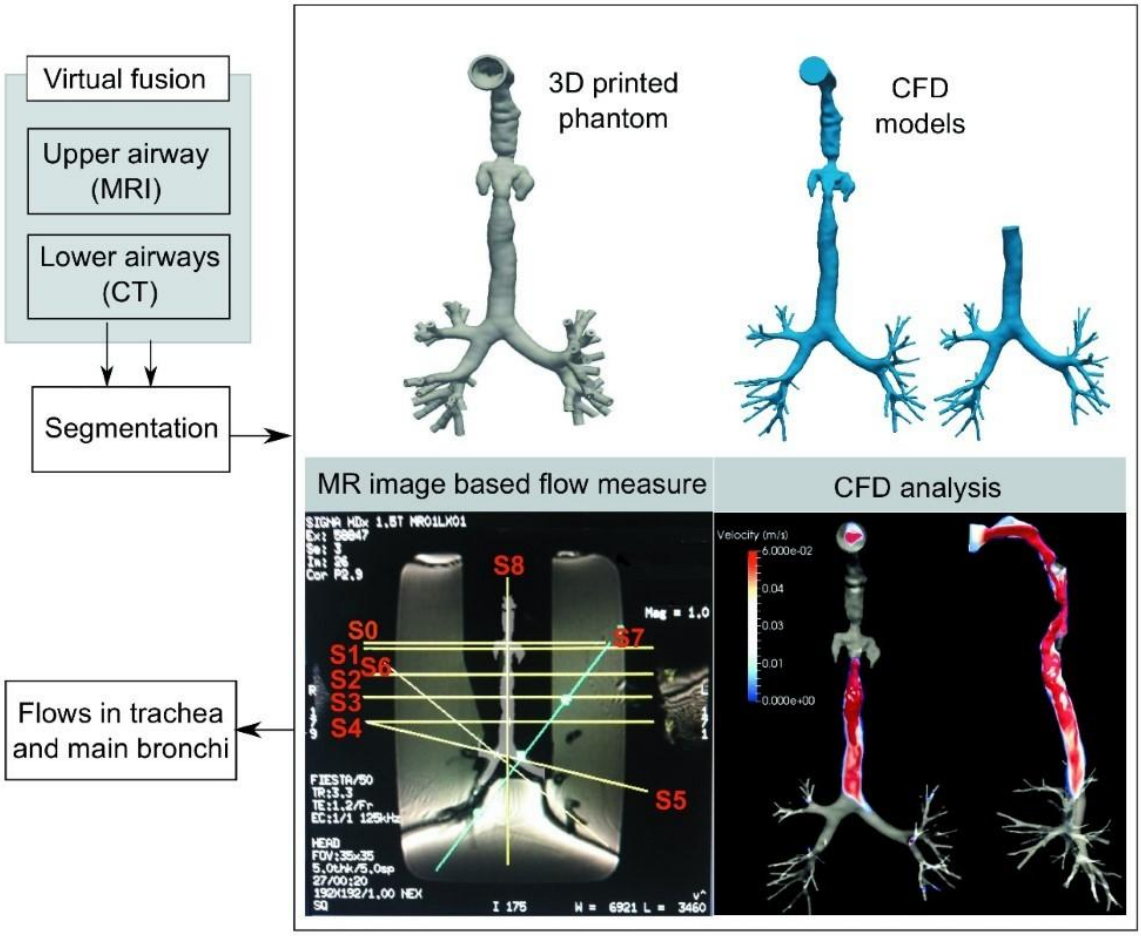
Virtual fusion
Upper airway (MRI)
Lower airways (CT)
Segmentation
Flows in trachea and main bronchi
3D printed phantom
CFD models
MR image based flow measure
CFD analysis
S0
S1
S2
S3
S4
S5
S6
S7
S8
Velocity (m/s)
6.000e-02
0.04
0.03
0.01
0.000e+00

Figure 2.

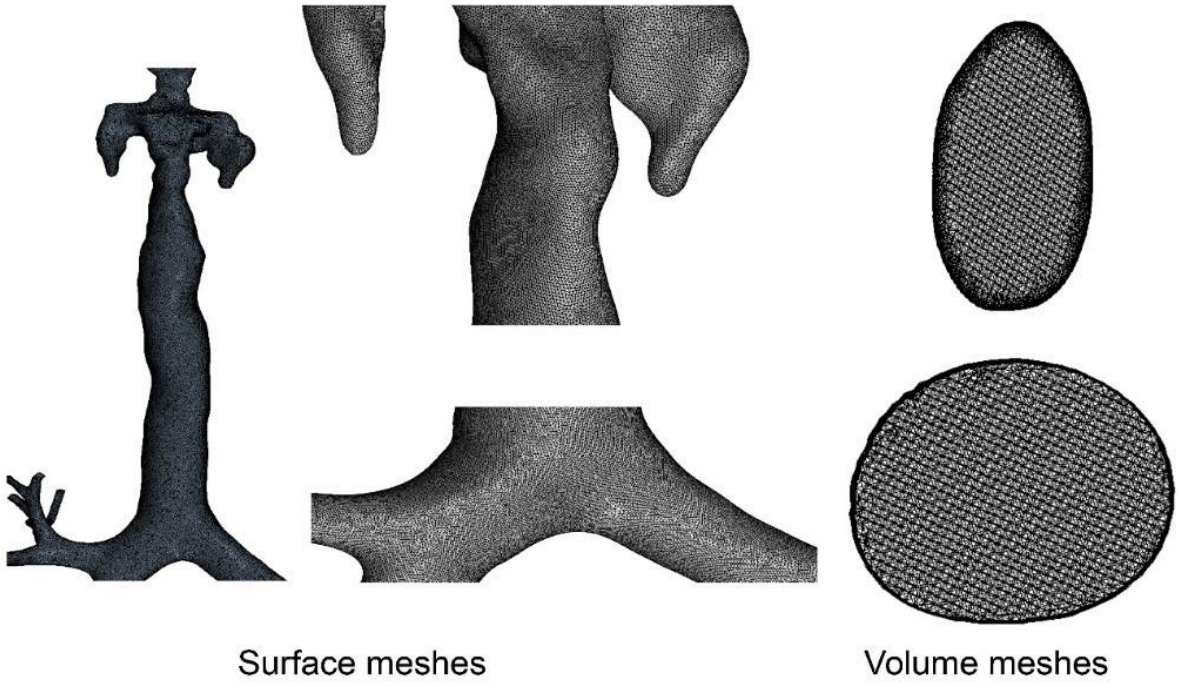

Figure 3.

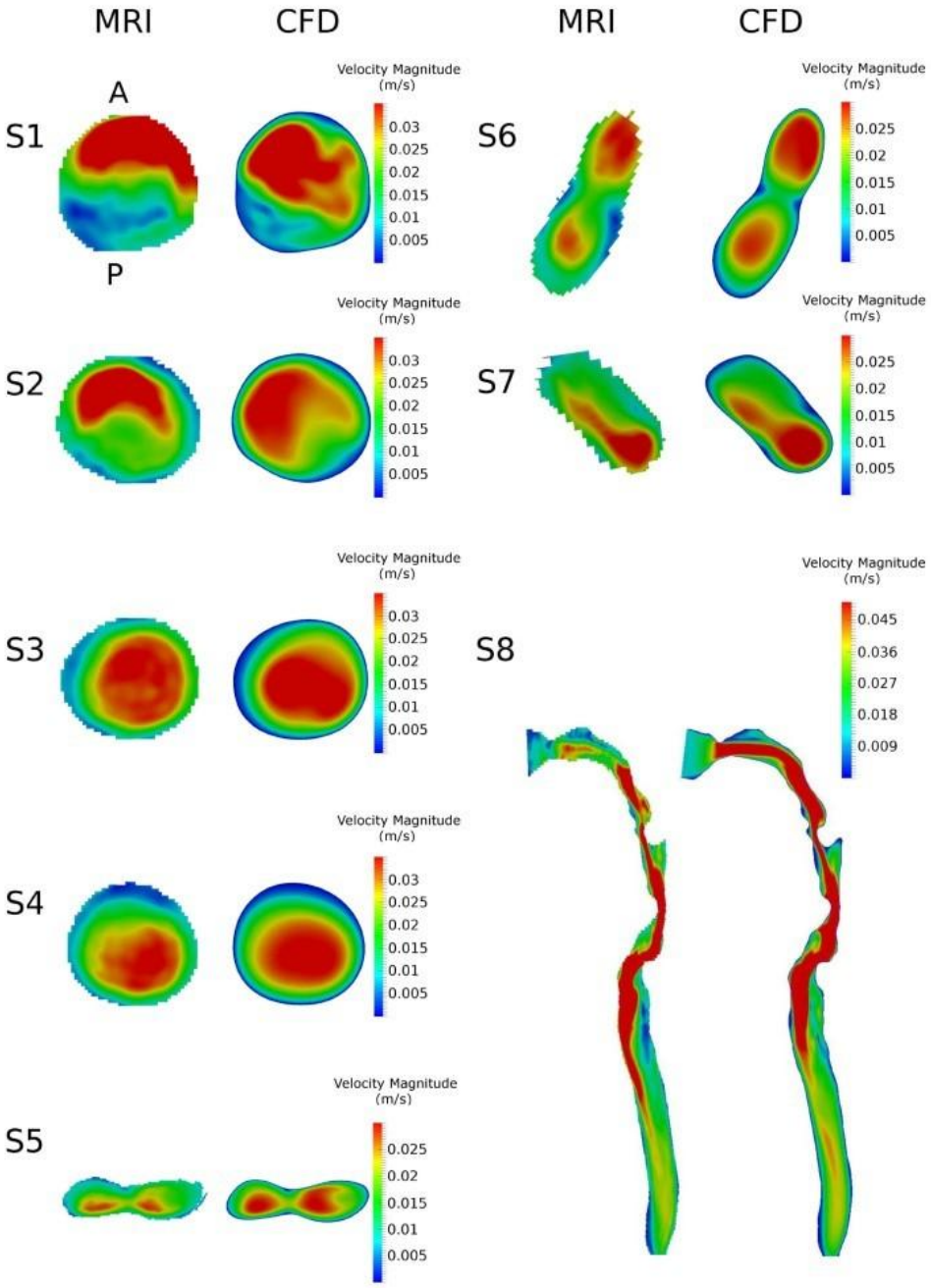
MRI
CFD
MRI
CFD
A
P
S1
S2
S3
S4
S5
S6
S7
S8
Velocity Magnitude (m/s)
0.03
0.025
0.02
0.015
0.01
0.005
0.045
0.036
0.027
0.018
0.009

Figure 4.

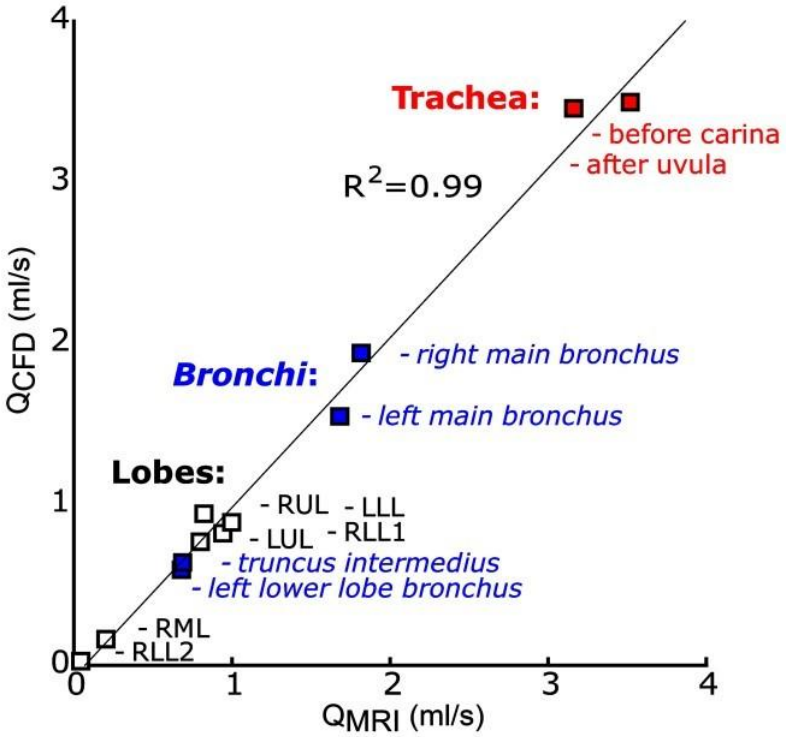
Trachea:
- before carina
- after uvula
R²=0.99
Bronchi:
- right main bronchus
- left main bronchus
Lobes:
- RUL
- LLL
- LUL
- RLL1
- truncus intermedius
- left lower lobe bronchus
- RML
- RLL2
QCFD (ml/s)
QMRI (ml/s)
0
1
2
3
4

Figure 5.

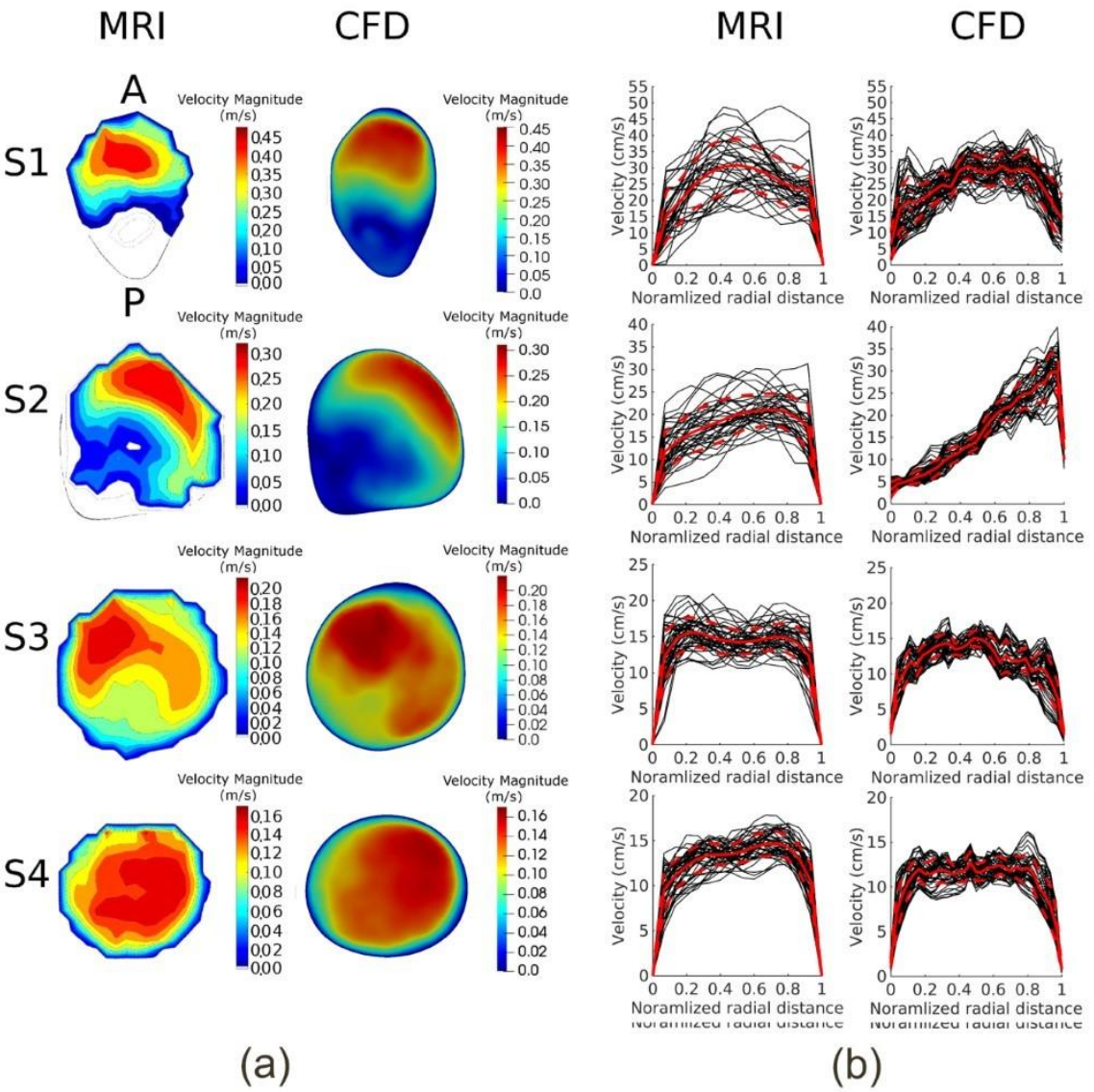
MRI
CFD
MRI
CFD
A
P
S1
S2
S3
S4
Velocity Magnitude (m/s)
Velocity (cm/s)
Noramlized radial distance
(a)
(b)

Figure 6.

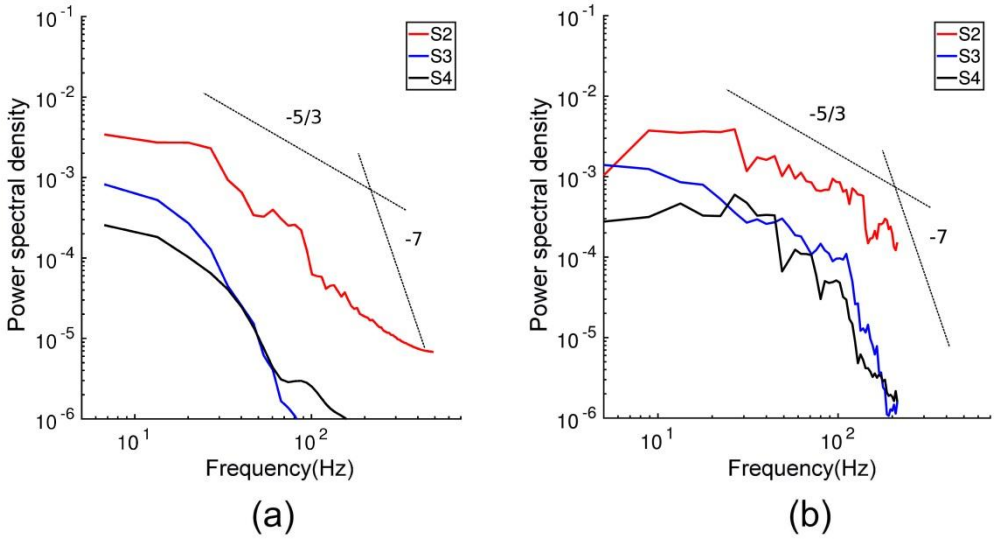

Figure 7.

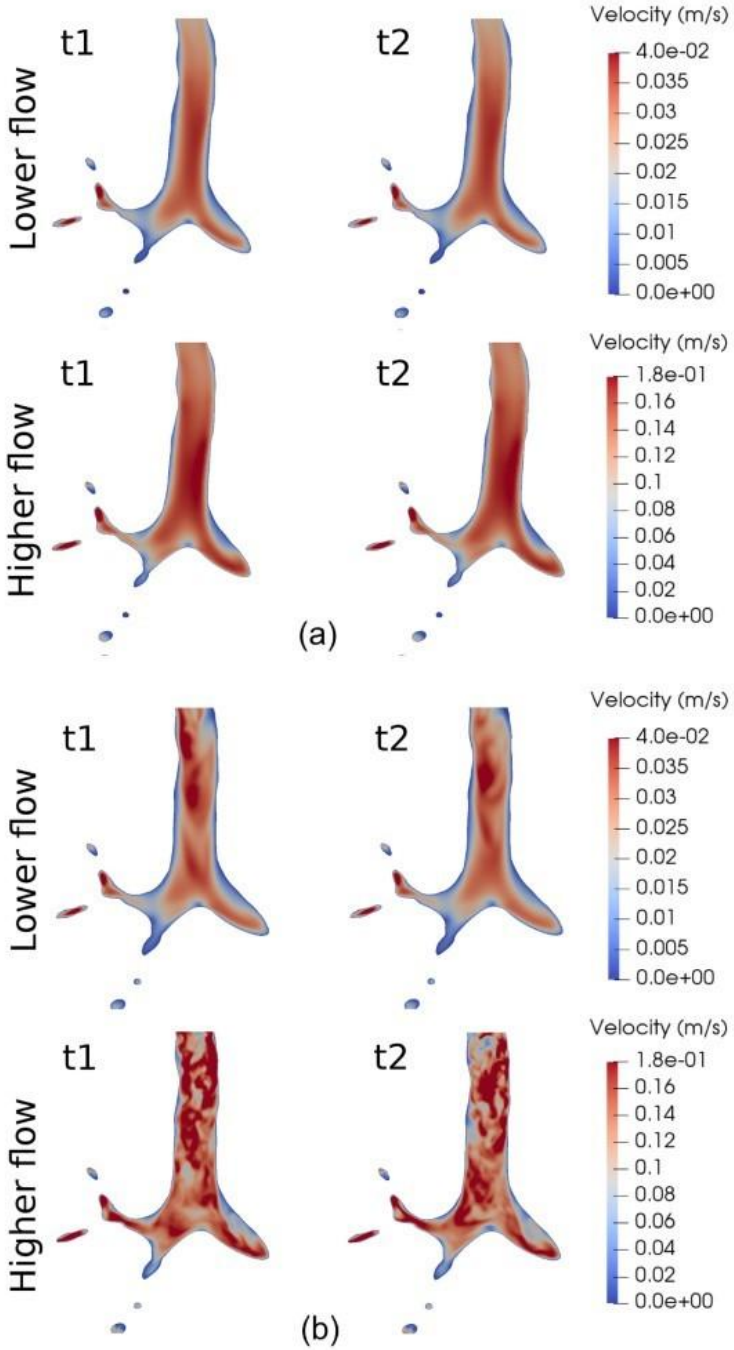
Lower flow
t1
t2
Velocity (m/s)
4.0e-02
0.035
0.03
0.025
0.02
0.015
0.01
0.005
0.0e+00
Higher flow
t1
t2
Velocity (m/s)
1.8e-01
0.16
0.14
0.12
0.1
0.08
0.06
0.04
0.02
0.0e+00
(a)
Lower flow
t1
t2
Velocity (m/s)
4.0e-02
0.035
0.03
0.025
0.02
0.015
0.01
0.005
0.0e+00
Higher flow
t1
t2
Velocity (m/s)
1.8e-01
0.16
0.14
0.12
0.1
0.08
0.06
0.04
0.02
0.0e+00
(b)

Figure 8.

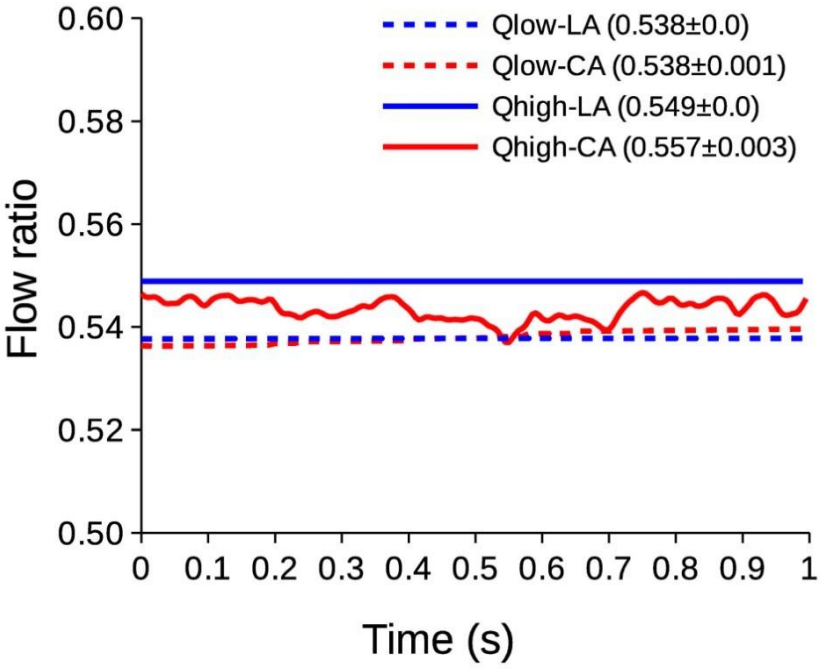
Qlow-LA (0.538±0.0)
Qlow-CA (0.538±0.001)
Qhigh-LA (0.549±0.0)
Qhigh-CA (0.557±0.003)
Flow ratio
0.60
0.58
0.56
0.54
0.52
0.50
0
0.1
0.2
0.3
0.4
0.5
0.6
0.7
0.8
0.9
1
Time (s)

Figure 9.

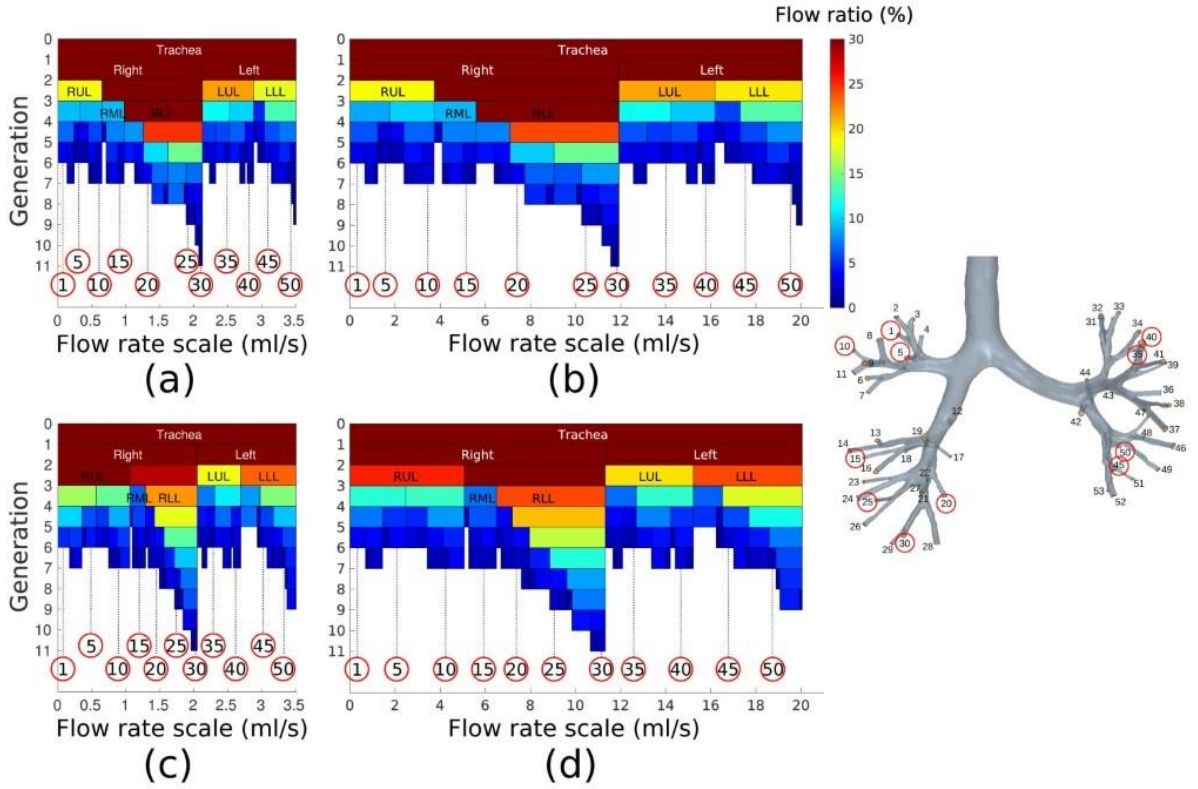
Flow ratio (%)
Trachea
Right
Left
RUL
RML
RLL
LUL
LLL
Generation
Flow rate scale (ml/s)
(a)
(b)
(c)
(d)

Figure 10.

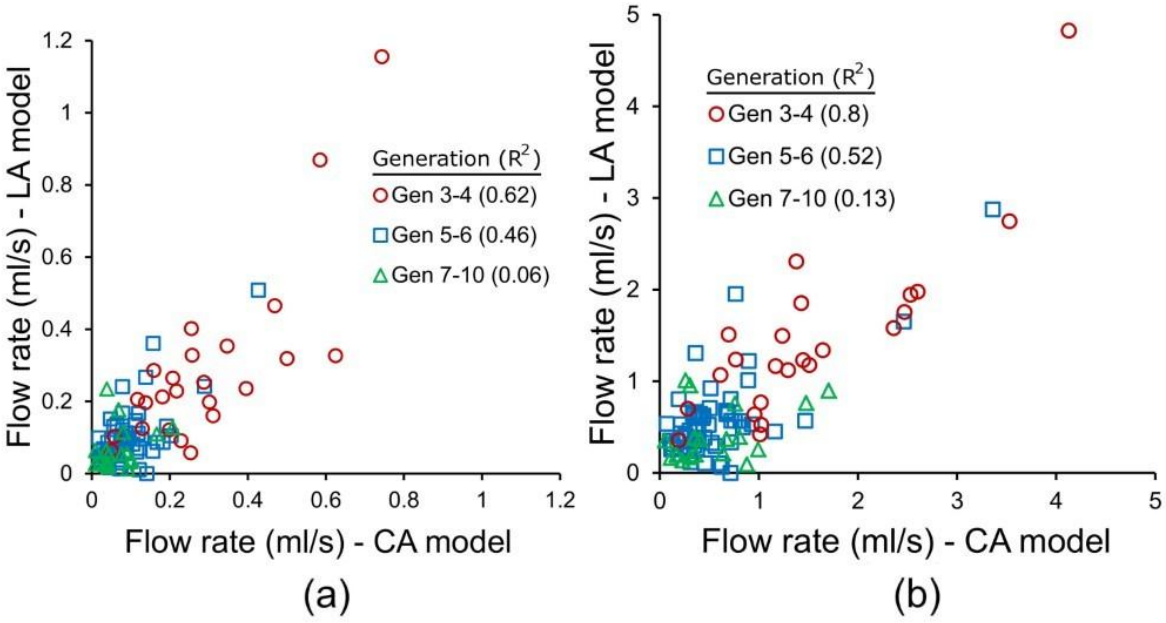
Flow rate (ml/s) - LA model
Flow rate (ml/s) - CA model
Generation (R^2)
Gen 3-4 (0.62)
Gen 5-6 (0.46)
Gen 7-10 (0.06)
(a)
Flow rate (ml/s) - LA model
Flow rate (ml/s) - CA model
Generation (R^2)
Gen 3-4 (0.8)
Gen 5-6 (0.52)
Gen 7-10 (0.13)
(b)